

Nanoscale tomographic reconstruction of the subsurface mechanical properties of low- k high-aspect ratio patterns

Gheorghe Stan,^{1,2*} Ebony Mays,³ Hui Jae Yoo,⁴ and Sean W. King³

¹*Material Measurement Laboratory, National Institute of Standards and Technology, Gaithersburg, MD 20899, USA*

²*School of Engineering and Applied Science, George Washington University, Washington, DC 20052, USA*

³*Logic Technology Development, Intel Corporation, Hillsboro, OR 97124, USA*

⁴*Components Research, Intel Corporation, Hillsboro, OR 97124, USA*

In this work, intermittent contact resonance atomic force microscopy (ICR-AFM) was performed on high-aspect ratio a-SiOC:H patterned fins (100 nm in height and width from 20 nm to 90 nm) to map the depth and width dependencies of the material stiffness. The spatial resolution and depth sensitivity of the measurements were assessed from tomographic cross-sections over various regions of interest within the 3D space of the measurements. Furthermore, the depth-dependence of the measured contact stiffness over the scanned area was used to determine the sub-surface variation of the elastic modulus at each point in the scan. This was achieved by iteratively adjusting the local elastic profile until the depth dependence of the resulted contact stiffness matched the depth dependence of the contact stiffness measured by ICR-AFM at that location. The results of this analysis were assembled into nanoscale sub-surface tomographic images of the elastic modulus of the investigated SiOC:H patterns. A new 3D structure-property representation emerged from these tomographic images with direct evidence for the alterations sustained by the structures during processing.

I. INTRODUCTION

The structure-property relationship of materials is essential in unlocking the development of new materials and applications, but access to the inner core of this multi-faceted interconnection was facilitated only recently by the development of 3D imaging techniques. The non-destructive 3D visualization of the internal structure of matter started about fifty years ago with the development of X-ray computed tomography¹⁻³ and is commonly used today in medicine, geophysics, and materials science. Besides simple visualization, the current requirements and road maps for nanoscale technologies ask for material property characterizations that can provide correlated structural and compositional 3D imaging at the nanoscale and beyond.⁴ In response to these demands, more and more quantitative physical and chemical 3D characterizations at this scale are enabled by either destructive imaging reconstruction (atom probe tomography⁵) or non-destructive near-field imaging techniques (atomic force microscopy,^{6,7} transmission electron microscopy,⁸⁻¹⁰ and near-field scanning optical microscopy^{11,12}).

In particular, 3D structure-property characterization is of increasing relevance in the semiconductor industry,^{4,13} where the achievement of desired functionalities is provided by the precise shaping and ordering of materials into component structures. As this control aims to advance toward the atomic limit, better optimization of the fabrication process is sought to be realized not only by dimensional metrology but also by various ma-

terial property characterizations with necessary spatial resolution.¹⁴⁻¹⁷ One good example here is the current state-of-the art of Cu-low- k dielectric interconnects in integrated circuits. Introduced about a decade ago to reduce the parasitic capacitive signal delays and power loss in transistors and metal-interconnect circuits, low- k dielectric materials experienced over years a continuous degradation of their mechanical properties.^{18,19} This mechanical deterioration was caused progressively by the increase in circuit density (due to difficulties associated with the dimensional patterning control at tighter and tighter pitches) and the reduction in the dielectric constant (the alterations made to reduce the dielectric constant usually happened at the expense of the mechanical rigidity of these materials). Consequently, as motivated by current and future technological demands,¹⁷ the effect of chemical composition and morphological structure on mechanical properties of low- k dielectric materials was under intense research in the last years, both theoretically and experimentally.¹⁸⁻²² However, the difficulties in testing their mechanical response became more and more challenging as the size of the specimens went from bulk to thin films and nanoscale high-aspect ratio patterns.

One viable solution to directly probe the local mechanics at the nanoscale is provided by various developed AFM-based techniques.²³⁻²⁸ Among these techniques, contact-resonance AFM (CR-AFM)^{29,30} demonstrated great potential for nanoscale quantitative elastic modulus measurements on various materials and structures. In particular, the versatility of CR-AFM in probing the nanoscale mechanical properties of dielectric thin films and interconnect circuits has been demonstrated in both spectroscopic and mapping modes.³¹⁻³⁴ In addition to that, intermittent CR-AFM (ICR-AFM)³⁵, an extension of CR-AFM, takes one step further in providing feasible means for subsurface nanoscale mechanical prop-

*To whom correspondence should be addressed: gheorghe.stan@nist.gov

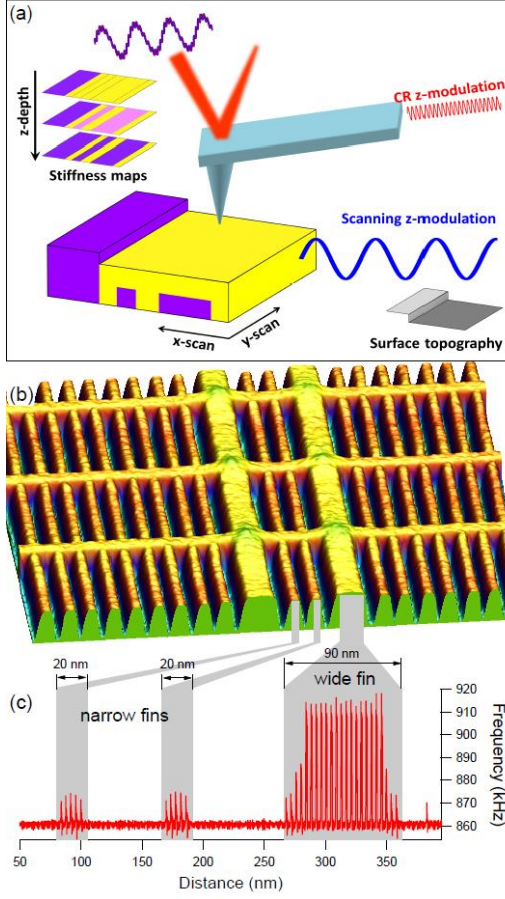


FIG. 1: (a) Schematic of ICR-AFM performed on an elastically inhomogeneous material showing the surface topography and the contrast variation that can be observed in the stiffness maps made at different depths. (b) 3D topographical view ($2\ \mu\text{m} \times 2\ \mu\text{m} \times 90\ \text{nm}$) of the low- k dielectric patterns investigated in this work; the patterns are referred as narrow fins (width 20 nm) and wide fins (width 90 nm). (c) Contact resonance frequency measured by ICR-AFM during scanning over the patterns shown in b). A change in the contact resonance frequency was measured at each tap only on the top of the fins as the tip was brought into contact from air to a maximum applied force of 60 nN.

erty characterization and complementing, in this regard, other dynamic AFM-based techniques^{7,36–43} for subsurface nanoscale characterization. In this work, ICR-AFM was used on high-aspect ratio low- k dielectric patterned fins to document an increase in mechanical stiffness at the top of the fins, namely a skin effect due to processing. The observations are based on the tomographic construction of the nanoscale 3D elastic modulus profile un-

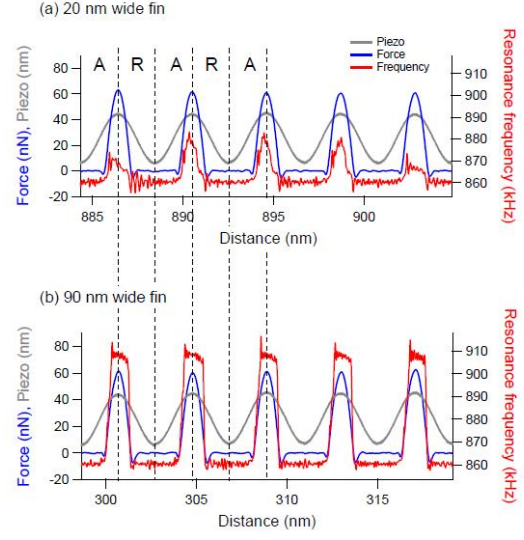


FIG. 2: Scanning z -modulation (piezo drive), applied force (cantilever deflection), and contact resonance frequency signals acquired during ICR-AFM scanning over (a) one of the narrow fins and (b) the middle part of one of the wide fins shown in Fig.1b. The letters A and R denote the approach and retract parts of the tapping cycles.

derneath the surface of these fins.

II. MATERIALS AND METHODS

The sample investigated in this work was in the form of a-SiOC:H high-aspect ratio patterns (refer to Fig. 1b), featuring geometries anticipated in the next generations of microprocessor interconnects. The patterns were defined by plasma enhanced chemical vapor deposition and subsequent plasma etching. The nano-porous low- k dielectric structures were fabricated using a previously described subtractive pitch quartering process.⁴⁴ Briefly, plasma enhanced chemical vapor deposition (PECVD) was used to deposit a 120 nm thick hybrid organic-inorganic silicate low- k dielectric on a 100 nm SiO_2 thin film previously grown on a 300 mm diameter Si(001) substrate. After deposition, the low- k dielectric was given a UV cure to liberate an intentionally incorporated sacrificial second phase organic pore building porogen resulting in a 33 % nanoporous dielectric.⁴⁵ The pitch quarter patterning process consisted of first depositing on the nano-porous dielectric a quad-layer film stack made of a backbone layer, an anti-reflection coating, a second backbone layer and a hard mask. Standard 193 nm immersion lithography and plasma etch techniques were utilized to form a grid pattern in the first backbone layer and transfer this pattern sequentially into the second backbone

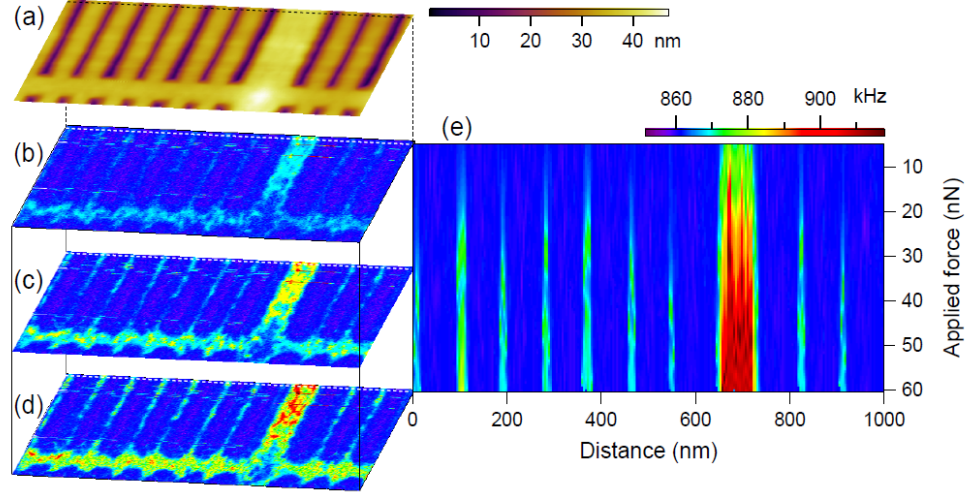


FIG. 3: (a) Surface topography of patterns comprising narrow and wide fins. (b), (c), and (d) Constant-load tomographic sections of the contact resonance frequency obtained from the ICR-AFM scanning made over the topography shown in a). The color contrast of the CR frequency sections shows the local variation in contact stiffness over the mapped areas at the corresponding applied force. (e) CR frequency versus force map along the scan line marked in a) by a dotted line. The spatial position of this map is also marked within the ICR-AFM 3D data by dotted lines in the sections shown in b), c), and d).

layer, the hard mask material, and nano-porous dielectric. On completion of transferring the pitch quartered pattern into the nano-porous dielectric, the remaining hard mask and plasma etch residues were removed using standard plasma ash and wet chemical cleans.

The resulted patterns resemble rectangular fins with widths of either 20 nm (referred as narrow fins) or 90 nm (referred as wide fins), spaced at 65 nm to each other, and about 100 nm in height (refer to Fig. 2b). Such delicate structures are hard to be imaged by AFM in contact mode and, therefore, are inaccessible for CR-AFM mapping. However, with ICR-AFM, operated in this case in peak-force tapping (PFT) (MultiMode Bruker AFM, Santa Barbara, CA, USA), the fins can be easily scanned, both in terms of surface topography (Fig. 1b) and CR mapping (Fig. 1c). ICR-AFM³⁵ pairs the measurement capability for depth-sensing contact stiffness of the conventional CR-AFM with the less-invasive surface probing of a force-controlled intermittent AFM mode. At each tap during ICR-AFM scanning, as the tip is pushed in and out of contact, the eigenmode frequencies of the cantilever vary with the induced change in the stiffness of the tip-sample contact. By tracking the variation of one of these contact resonance frequencies as a function of indentation depth at each point in the scan, a 3D data volume is generated; such data set provides a tomographic representation of the sub-surface stiffness field of the sample. A schematic of ICR-AFM measurements is shown in Fig. 1a with the highlight of how the topographic features and sub-surface heterogeneities can be assessed in

successive tomographic slices.

In the AFM topography image (Fig. 1b), the fins appear enlarged toward the bottom of the trenches due to the tip-sample convolution, yet the CR-AFM signal (Fig. 1c) clearly shows the lateral extent of these fins because no CR-AFM detection was made in between them. A first interpretation of the measurements shown in Fig. 1c would be that the wide fins exhibit an increased contact stiffness in comparison with the narrow fins because larger contact resonance frequencies were measured on the wide fins than on the narrow ones at the same applied forces. The statement, however, is incomplete if we think in terms of intrinsic elastic properties of materials. This is because the contact stiffness depends on the contact geometry and the observed reduction in contact stiffness (i.e. contact resonance frequencies in Fig. 1c) on the narrow fins and around the edges of the wide fins includes a large contribution from edge compliances. It is thus necessary to perform a detailed analysis to properly convert the measured contact stiffness into elastic modulus.

For the ICR-AFM measurements presented in this work, the AFM probe used was a PPP-SEIH probe (Nanosensors, Neuchatel, Switzerland) with the first two free-eigenmode frequencies at 111.5 kHz and 722.6 kHz, and a spring constant of 8.1 ± 0.5 N/m (as measured by the thermal tune method of the AFM). The scanning was performed at $1 \mu\text{m/s}$ speed with the PFT modulation (Bruker, Santa Barbara, CA, USA) in the form of a sinusoidal oscillation at 0.25 kHz and 15 nm amplitude. A

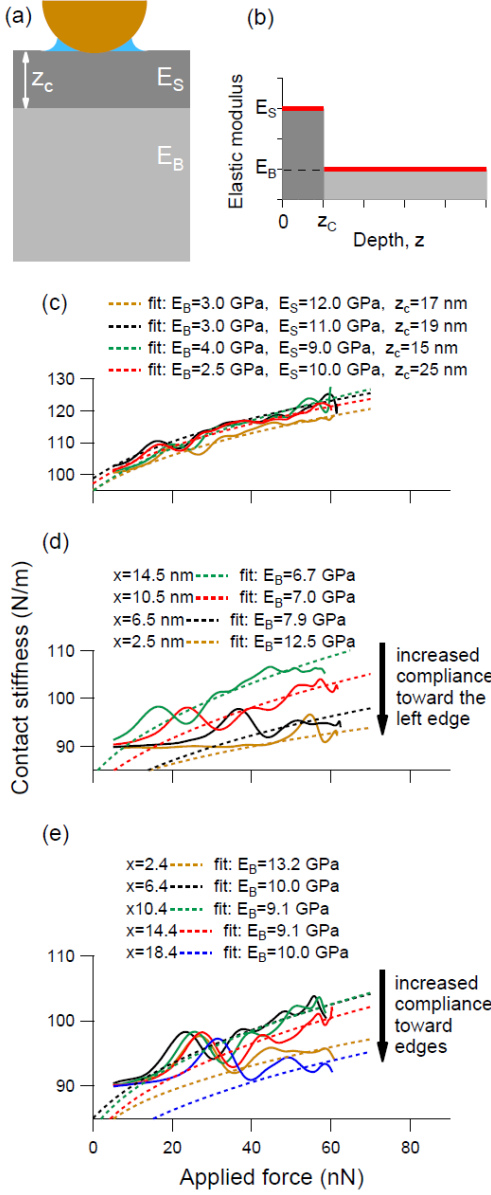


FIG. 4: (a) Spherical tip indenting a coated substrate (a homogeneous top layer of thickness z_c over a homogeneous substrate) in the presence of adhesion. (b) The elastic profile of the indented structure is considered as a step function, with constant elastic moduli E_S and E_B for the coat and substrate, respectively. Measured (solid curves) and fitted (dotted curves) dependencies of the contact stiffness versus applied force (c) at a few locations in the middle and (d) at one of the edges of the wide fin shown in Fig. 3e, and (e) across one of the narrow fins shown in Fig. 3e. The positions x are measured from the left edge of the fin; refer to text for details.

phase-locked loop system (SPECS Zurich GmbH, Zurich, Switzerland) was used in constant excitation-mode (20 mV drive amplitude) to track the frequency changes within a 78.1 kHz frequency-window centered around 860.6 kHz. All uncertainties reported here and in the text represent one standard deviation of the calculated values.

III. RESULTS AND DISCUSSION

The calculation of the elastic modulus makes use of all the measured signals: scanning z -modulation (PFT piezo modulation) for lateral position, applied force (cantilever deflection) for vertical position and indentation state, and CR frequency for contact stiffness.⁴³ Short sequences of these signals are detailed in Fig. 2 for measurements over one of the narrow fins and the middle part of one of the wide fins. As can be seen, the changes in the CR frequency during tapping were measured in stable scanning conditions; neither the piezo signal nor the cantilever deflection (with feedback control on the maximum applied force) showed any perturbations over either the narrow or wide fins. The correlation between contact stiffness and applied force at any location in the scan is used to infer the applied force dependence of the contact stiffness.

By using their space locations (x and y for in-plane positions and z for applied force), the ICR-AFM measurements were assembled in a 3D volume of data (Fig. 3), being possible to slice off tomographic sections along any direction. In the left panel of Fig. 3 are shown CR frequency maps at a few applied forces. The maps exhibit a very good correlation with the topography of the sample (shown on top of the CR frequency maps) and local variations in the stiffness, both across and along the patterns, can be identified over the mapped area. Conversely, a tomographic section along a scan line shows the variation in stiffness with the applied force (refer to Fig. 3e) and distinctively highlights the edge effect at the edges of the wide fin and over the narrow fins. The force dependence of the CR frequency in such maps will be used in the following to retrieve the sub-surface elastic modulus profile of the patterns.

The construction of the 3D elastic modulus tomography from ICR-AFM measurements consists of an inverse problem, which is to find the elastic profile over the sensed depth in such a way that the calculated stiffness response of the material probed will match the depth dependence of the measured contact stiffness. This means that, unlike X-ray tomography where the structures of interest are directly imaged at different focal planes within the scanned volume, the sectional planes of ICR-AFM contact stiffness at a given depth (obtained from maps as those shown in the left panel of Fig. 3) contain the integral response of the material probed by the AFM tip over the indentation depth. Moreover, it is not contact stiffness but the elastic modulus at the probed depth that

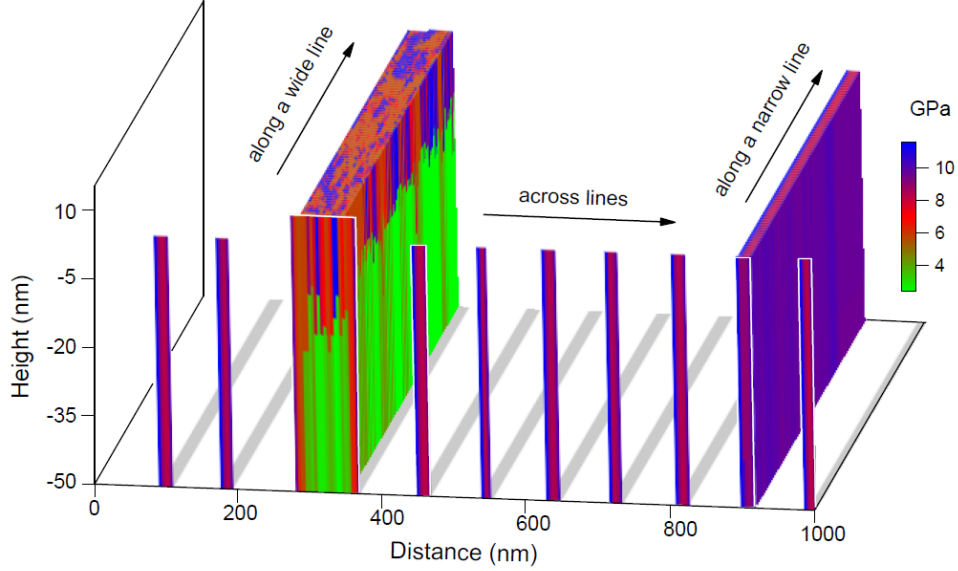


FIG. 5: (a) Tomographic sections of the calculated elastic modulus of the fins. Lateral and vertical variations in the elastic modulus are observed in both front-view (across the fins) and depth-view (along the fins) sections. The locations of the fins are marked by gray traces in the basal plane; these locations were identified from CR-AFM measurements and AFM signals (piezo, cantilever deflection) on top of the fins.

represents an intrinsic material property at that particular depth in the structure. It is by the use of a contact model that the actual 3D profile of the elastic modulus within the volume probed is recovered as the source of the measured contact stiffness. Moreover, as discussed in the following, the selection of the contact model has to be made in accordance with the structure of the material probed and the measurement contact geometry.

During various processing stages (addition of porosity, lithography, curing, etc.) when the required properties and patterns are devised, the low- k dielectric materials and especially their defined interfaces sustain chemical and structural modifications,^{18,46} which in turn alter the mechanical rigidity of these materials toward their exposed surfaces, i.e. a superficial stiffening of the processed interfaces. Such sub-surface inhomogeneities were revealed in nanoscale optical⁴⁷ and mechanical^{32,34} measurements of blanket and patterned films. To analyze the increase in the superficial stiffness of the ILD structures investigated in this work, a non-uniform profile for the elastic modulus of the fins was considered. Thus, as illustrated in Fig. 4a and Fig. 4b, the fins were modeled as made of two homogeneous parts, a stiffer cap layer of modulus E_S and thickness z_c at the top of the fins and

a bulk part of modulus E_B for the base of the fins:

$$E(z) = \begin{cases} E_S & \text{for } 0 \leq z \leq z_c \\ E_B & \text{for } z > z_c \end{cases}, \quad (1)$$

with $z = 0$ at the free surface of the fins. Other profiles (e.g. linear, multi-steps, exponential, etc.) could be considered to describe the sub-surface gradient of the elastic modulus of these structures.

Based on the above assumptions for the sub-surface structural inhomogeneity and considering the effect of adhesion to the tip-sample contact, the appropriate description for the contact configuration will be that of a spherical tip indenting a flat surface of a single-layer coated homogeneous half-space in the presence of adhesion (refer to Fig. 4a). The contribution of adhesive forces to the tip-sample contact was included in the present analysis because the measurements were performed on compliant materials in ambient atmosphere (45 % relative humidity and 21 °C) and at relatively small applied forces (maximum applied force of 60 nN). In the contact model used,^{48,49} the adhesive interaction between the indenter and the contacted surface is treated as Maugis-type adhesion,⁵⁰ which is in the form of a uniform tensile stress σ_0 within an annular adhesive region surrounding the contact zone, $a < r < c$ (a is the contact radius, r is the radial coordinate in the surface's plane with the origin at the intersection between the axis of the indenter and the

surface's plane, and c is the adhesion radius). Furthermore, as indicated by measurement conditions and subsequent analysis, the tip-sample adhesion operated and was described in the Johnson-Kendall-Roberts (JKR) limit⁵¹ of the adhesive range of the Maugis model; in general, JKR limit describes adhesive contacts on compliant materials with large contact radius.

By following the Maugis model,⁵⁰ the indentation depth δ can be calculated from the surface displacement $u_z(r)$ and the tip-shape function $r^2/2R_T$ as

$$\delta = u_z(r) + r^2/2R_T, \quad (2)$$

with R_T being the tip radius. As detailed in references⁴⁸ and⁴⁹, an integral transform formulation is used then to resolve the adhesive contact between a spherical tip and either a single-layer or multiple-layer coated substrate, respectively. In short, for a given contact radius a , the stress distribution and contact radius ratio c/a (determined by the adhesive forces) are adjusted iteratively until the displacement equations at $r = a$ and $r = c$ (equation (2)) are satisfied simultaneously. Once the stress distribution $\sigma_z(r)$ inside the contact region is determined, it can be used to calculate the total contact load (including the contribution from adhesion):

$$F = - \left[\int_0^a \sigma_z(r) 2\pi r dr + \sigma_0 \pi c^2 \right]. \quad (3)$$

By combining the two above equations, the force dependence of the indentation depth is obtained and the contact stiffness can be calculated as the derivative of the load with respect to the indentation depth, $\partial F/\partial \delta$; moreover, for the purpose of our data analysis, the contact stiffness versus contact load is also retrieved from this procedure.

The above derivation for the contact stiffness holds for static and quasi-static indentations on rather stiff materials. However, as described in previous works,^{43,52} the dynamic stiffness response of an elastomer indented by a spherical tip resembles that of a “flat-punch” contact configuration (an indenter with circular flat end of radius equal with the contact radius of the static configuration). Therefore, for every contact radius a , the contact stiffness was calculated for the “flat-punch” configuration of that radius,

$$k^*(F) = \partial F_{\text{punch}}/\partial \delta_{\text{punch}}|_{a=a(F)}, \quad (4)$$

by using the force-displacement curve of a flat-punch of radius a indenting the considered single-layer coated substrate.⁵³ This contact stiffness k^* is well-defined for an indented half-space, far away from any edge. In addition to that, an increase in the compliance of the system has to be considered in our case for the indents located in the proximity of an edge. Such edge effects are observed in the decay of the CR frequencies measured toward the edges of the wide fin and across narrow fins (refer to Fig. 1c). Therefore, the total compliance of a fin, at a distance

x from the edge,

$$\frac{1}{k_{\text{fin}}} = \frac{1}{k^*} + \frac{1}{k_{\text{edge}}}, \quad (5)$$

includes the compliance of the inner (non-edge) part, $1/k^*$, and the edge compliance $1/k_{\text{edge}} = C_{\text{edge}}/(E^*x)$,⁵⁴ with C_{edge} constant and $E^* = k^*/(2a)$ the reduce elastic modulus of the tip-sample contact. When both edges (one edge at $x = 0$ and one edge at $x = w$) are contributing, the force and x -position dependence of the total compliance of a fin of width w becomes

$$\frac{1}{k_{\text{fin}}(F, x)} = \left[1 + C_{\text{edge}} \frac{w}{x(w-x)} 2a(F) \right] \frac{1}{k^*(F)}. \quad (6)$$

The general form of $k_{\text{fin}}(F, x)$ given by equation (6) was used to analyze the force and edge dependence of the measured contact stiffnesses over the low- k dielectric fins imaged in this work. The numerical calculations for the above derivation follow the algorithms developed in references^{48,49,53}.

At locations over the wide fin, far away from edges, the fit parameters, E_B , E_S , and z_c , were adjusted until the calculated force dependence of the contact stiffness matched the measurements with at least 90 % coefficient of determination R-squared. For the fits over the narrow fins and edges of the wide fin, it was observed that consistent results were obtained for a homogeneous structure of the fin, namely $E_B = E_S = E(z_c = 0)$; also, for these fits, the considered range for force was restricted to applied forces above 30 nN, where the contact stiffness showed a clear sensitivity to the applied force. The tip radius R_T necessary for these calculations was found by deconvoluting the tip geometry from the AFM topographical profile across the fins. This was done by simulating the convoluted contact between a circle of adjustable radius as it is rolled over rectangular shapes that have the geometrical dimensions and spatial distribution of the scanned fins (see Supplementary data for details). The best fit for the average AFM profiles over a series of narrow and wide fins provided a tip radius of 67 ± 2 nm; the uncertainty was not considered in the subsequent calculation of the elastic modulus.

Based on the above considerations for contact mechanics and fit procedure, a few examples showing fits of the contact stiffness measurements are presented in Fig. 4. Fig. 4c shows measurements and calculations at a few locations across the wide fin, far from any edge. As can be seen, the general force dependence of the measured contact stiffness is reproduced over the entire range of applied forces. For a given value of the bulk elastic modulus, E_B , the increase in contact stiffness at low applied forces is regulated by the magnitude of the surface elastic modulus, E_S , and the transition regime from lower to higher forces reveals the extent of the top stiffer layer, namely, the value of z_c . In the absence of this stiffer cap layer, a much steeper increase in contact stiffness with the applied force would have been observed; the mea-

sured force-contact stiffness dependencies were not reproduced by fits that considered homogeneous indented materials (see Supplementary data for comparison between fits with variable and constant elastic modulus). It is also notable that the elastic modulus of the “bulk” part, E_B , was found from these fits to be around 3.5 GPa, which is close to the elastic modulus 3.0 GPa determined from CR-AFM measurements³⁴ on blanket films made of the same low- k material as the patterns investigated in this work. This correlation confirms the ability of ICR-AFM to recover correctly the depth dependence of the elastic profile underneath the surface probed.

Force-contact stiffness curves at locations close to one of the edges of the wide fin and across one of the narrow fins are shown in Figs. 4d and 4e, respectively. The edge effect on the curves shown in Fig. 4d manifests as an overall reduction in contact stiffness (increase compliance) as the measurement location shifts closer and closer to the edge. In Fig. 4e, the lowest curves are for measurements on each edge of the narrow fin and the highest curves at positions around the middle part of the fin; the position of each measurement with respect to the left edge of the fin is specified by x . In addition to E_B , E_S , and z_c , C_{edge} was considered as a fit parameter for curves showing edge effects. The constant C_{edge} was obtained by simultaneously fitting the stiffness measurements made on each side of the wide fin. This means that the same value was obtained for C_{edge} from each set of the three or four measurements showing edge effect along the edges of the wide fin; only one edge was considered to contribute to the measurements made around each edge of the wide fin. The value of C_{edge} was then used to fit the measurements made on the narrow fins, in which case both edges were considered to contribute to the total compliance of a fin (equation 6). As can be seen from the values of the fit parameters, elastic moduli as big as three times of that of the inner part of the wide fin were determined for the top and sidewalls of the wide fin and for the entire volume of the narrow fins. This is in apparent contradiction with the stiffness decay predicted by CR measurements over the narrow fins (Figs. 1c and 3), prior to the analysis that includes the edge effects. The highlight here is that the stiffness increase of the exposed surfaces of the fins is revealed once the contribution of edge compliances to the measurements is properly accounted for. It should be also noted that occasional bursts are present in the contact stiffness vs force measurements, especially at small forces near the edges of the wide fin (Fig. 4d) and on narrow fins (Fig. 4e). One main source of these disturbances could be the increased compliance of the tip-sample contact around edges and a noise reduction might be achieved at higher loads. However, it is worth pointing out that all the measurements were performed in the elastic deformation regime of the materials as indicated by the calculated contact stresses (see Supplementary data for details) and absence of plastic deformation of the samples at the nanoscale. Thus, the maximum compressive stress induced at an applied

force of 60 nN is around 0.6 GPa, which is below the estimated yield strength of these organo-silicate materials. The estimate is based on the yield stress measurements of SiCH/SiOCH bilayers⁵⁵ with the SiOCH layers having similar structure and properties (porosity 25 % and elastic modulus 8.0 GPa) to our materials. In these measurements it was found that the top SiCH layers can accommodate yield stresses as high as 1.0 GPa depending on their porosity. Based on the observation that plasticity was always initiated in the top SiCH layer of the structure we can conclude that the yield stresses of the SiOCH layers are even higher than those of the SiCH layers.

To get a better perception and statistics of the elastic properties of the investigated structures, tomographic sections of the calculated elastic moduli of the fins were made and are shown in Fig. 5. The front-view section shows the elastic modulus variations across one wide fin and a few narrow fins and the depth-view sections map the elastic modulus variations along the wide fin (the edge regions were not included) and one of the narrow fins. In general, as can be seen from the color code of the elastic modulus, an increase in stiffness (bigger elastic modulus) was determined in the regions adjacent to the exposed top and side surfaces of the fins. On the wide fin this stiffer region forms a top layer about 20 nm in thickness and extends inwards about 15 nm from the sides. The narrow fins, on the other hand, indicate only one uniform, stiffer region over their entire volume, probably because the width of the narrow fins is comparable with the penetration depth of the stiffer region. It is interesting also that less variations and slightly bigger modulus values were determined along the narrow fins than within the cap layer of the wide fin. The statistics of the fit parameters along the wide fin indicate average values of 3.4 ± 0.8 GPa for E_B , 7.9 ± 2.2 GPa for E_S , and 20.3 ± 5.2 nm for z_c . Along the narrow fin, the fits gave 9.8 ± 1.7 GPa for the elastic modulus E . It is indicative here that the elastic modulus of the inner parts of the wide fins is comparable with that of the porous low- k films (3.0 GPa)³⁴ whereas the elastic modulus of their exposed surfaces (tops and sidewalls) approaches the modulus of the organosilicate matrix of these films (7.3 GPa).³⁴ Also, the thicknesses of the top and side stiffer regions are comparable with the damaged sidewalls of ILD structures exposed to plasma; it has been shown by either selective etch,⁵⁶ ellipsometry,⁵⁷ or transmission electron microscopy⁵⁸ that a 20 nm to 50 nm oxidized region can be formed at the sidewall of an ILD where, under the action of plasma ash, non-polar methyl CH_3 groups are replaced by polar silicon hydroxide $\text{Si}-\text{OH}$ groups. Therefore, both the measured elastic moduli of the inner and exposed surfaces and the extend of the stiffened regions of the investigated fins confirmed the nanoscale effect of processing on low- k dielectric materials. In previous studies, it has been shown that the chemical composition of the sidewall is different from that of the bulk part. Here we directly probed the alteration in

the mechanical properties of the top and sidewall regions.

IV. CONCLUSIONS

In this work, a process-induced stiffened region was demonstrated for the exposed surfaces (top and sides) of high-aspect ratio ILD patterns. The sub-surface variations of the mechanical properties of these patterns were mapped by 3D ICR-AFM across 20- and 90-nanometer wide patterns. The detailed depth-dependence of the measured ICR-AFM contact stiffnesses allowed the use of a contact model with three fit-parameters to unveil the elastic modulus profile underneath the surface. By combining AFM topography and ICR-AFM measurements, tomographic sections of the elastic modulus across features of interest were generated and used to demonstrate the stiffness enhancement sustained by the ILD patterns

during processing. Roughly, an increase by a factor of three was calculated for the elastic modulus within a 20 nm thickness from the exposed surface. Applications of such nanoscale near-surface mechanical interrogations can be envisioned for other materials with inhomogeneous superficial layers, either inorganic (nanoelectronics, coatings, composite materials, etc.) or organic (teeth, bones, hydrogels, tumors etc.).

Conflict of Interest: The authors declare no competing financial interest.

Disclaimer. Certain commercial equipment, instruments or materials are identified in this document. Such identification does not imply recommendation or endorsement by the National Institute of Standards and Technology or Intel Corporation, nor does it imply that the products identified are necessarily the best available for the purpose.

- ¹ Cormack A M 1963 Representation of a function by its line integrals with some radiological applications *J. Appl. Phys.* **34** 2722-7
- ² Hounsfield G N 1973 Computerized transverse axial scanning (tomography): Part 1. Description of system *Br. J. Radiol.* **46** 1016-22
- ³ Goldman L W 2007 Principles of CT and CT Technology *J. Nucl. Med. Technol.* **35** 115-28
- ⁴ Muller D A 2009 Structure and bonding at the atomic scale by scanning transmission electron microscopy *Nature Mater.* **8** 263-70
- ⁵ Blavette D, Bostel A, Sarrau J M, Deconihout B and Menand A 1993 An atom probe for three-dimensional tomography *Nature* **363** 432-5
- ⁶ Albers B J, Schwendemann T C, Baykara M Z, Pilet N, Liebmann M, Altman E I and Schwarz U D 2009 Three-dimensional imaging of short-range chemical forces with picometre resolution *Nature Nanotechnol.* **4** 307-10
- ⁷ Herruzo E T, Asakawa H, Fukuma T and Garcia R 2013 Three-dimensional quantitative force maps in liquid with 10 piconewton, angstrom and sub-minute resolutions *Nanoscale* **5** 2678-85
- ⁸ De Rosier D J and Klug A 1968 Reconstruction of three dimensional structures from electron micrographs *Nature* **217** 130-4
- ⁹ Porter A E, Gass M, Muller K, Skepper J N, Midgley P A and Welland M 2007 Direct imaging of single-walled carbon nanotubes in cells *Nat. Nanotechnol.* **2** 7137
- ¹⁰ Midgley P A and Dunin-Borkowski R E 2009 Electron tomography and holography in materials science *Nature Mater.* **8** 271-80
- ¹¹ Lewis A, Taha H, Strinkovski A, Manevitch A, Khatchourians A, Dekhter R and Ammann E 2003 Near-field optics: from subwavelength illumination to nanometric shadowing. *Nature Biotechnol.* **21** 1378-86
- ¹² Taubner T, Keilmann F and Hillenbrand R 2005 Nanoscale-resolved subsurface imaging by scattering-type near-field optical microscopy *Optics Express* **13** 8893
- ¹³ Kelly T F, Larson D J, Thompson K, Alvis R L, Bunton J H, Olson J D and Gorman B P 2007 Atom probe tomography of electronic materials *Annu. Rev. Mater. Res.* **37** 681727
- ¹⁴ Chau R, Doyle B, Datta S, Kavalieros J and Zhang K 2007 Integrated nanoelectronics for the future *Nature Mater.* **6** 810-2
- ¹⁵ Busch B W, Pluchery O, Chabal Y J, Muller D A, Opila R L, Kwo J K and Garfunkel E 2002 Materials characterization of alternative gate dielectrics *MRS Bull.* **27** 206-11
- ¹⁶ Galatsis K, Potok R and Wang K L 2007 A review of metrology for nanoelectronics *IEEE Transactions on semiconductor manufacturing* **20** 542-8
- ¹⁷ King S W, Simka H, Herr D, Akinaga H and Garner M 2013 Research Updates: The three Ms (materials, metrology, and modeling) together pave the path to future nanoelectronic technologies *APL Materials* **1** 040701
- ¹⁸ Baklanov M R, de Marneffe J -F, Shamiryan D, Urbanowicz A M, Shi H, Rakhimova T V, Huang H and Ho P S 2013 Plasma processing of low-*k* dielectrics *J. Appl. Phys.* **113** 041101
- ¹⁹ Vanstreels K, Wu C and Baklanov M R 2015 Mechanical stability of porous low-*k* dielectrics *ECS J. Solid State Sci. Technol.* **4** N3058-64
- ²⁰ Maex K, Baklanov M R, Shamiryan D, Iacopi F, Brongersma S H and Yanovitskaya Z S 2003 Low dielectric constant materials for microelectronics *J. Appl. Phys.* **93** 8793-841
- ²¹ Urbanowicz A M, Vanstreels K, Verdonck P, Van Besien E, Christos T, Shamiryan D, De Gendt S and Baklanov M R 2011 Effect of UV wavelength on the hardening process of porogen-containing and porogen-free ultralow-*k* plasma-enhanced chemical vapor deposition dielectrics *J. Vac. Sci. Technol. B* **29** 032201-9
- ²² Li H, Lin Y, Tsui T Y and Vlassak J J 2009 The effect of porogen loading on the stiffness and fracture energy of brittle organosilicates *J. Mater. Res.* **24** 107-16
- ²³ Rodriguez T R and Garcia R 2004 Compositional mapping of surfaces in atomic force microscopy by excitation of the second normal mode of the cantilever *Appl. Phys. Lett.* **84** 44951
- ²⁴ Sahin O, Magonov S, Su C, Quate C F and Solgaard O

- 2007 An atomic force microscope tip designed to measure time-varying nanomechanical forces *Nature Nanotechnol.* **2** 507-14
- 25 Jesse S, Kalinin S V, Proksch R, Baddorf A P, and Rodriguez B J 2007 The band excitation method in scanning probe microscopy for rapid mapping of energy dissipation on the nanoscale *Nanotechnology* **18** 435503
 - 26 Pittenger B, Erina N and Su C 2012 Quantitative Mechanical Property Mapping at the Nanoscale with PeakForce QNM *Bruker Application Note* **128**
 - 27 Raman A, Trigueros S, Cartagena A, Stevenson A P Z, Susilo M, Nauman E and Contera S A 2011 Mapping nanomechanical properties of live cells using multiharmonic atomic force microscopy *Nat. Nanotechnol.* **6** 80914
 - 28 Garcia R and Herruzo E T 2012 The emergence of multi-frequency AFM *Nature Nanotechnol.* **7** 21726
 - 29 Rabe U, Janser K and Arnold W 1996 Vibrations of free and surface-coupled atomic force microscope cantilevers: Theory and experiment *Rev. Sci. Instrum.* **67** 3281-93
 - 30 Yamanaka K and Nakano S 1996 Ultrasonic atomic force microscope with overtone excitation of cantilever *Japan. J. Appl. Phys.* **35** 3787-92
 - 31 Stan G, King S W and Cook R F 2009 Elastic modulus of low- k dielectric thin films measured by load-dependent contact-resonance atomic force microscopy *J. Mater. Res.* **24** 2960-4
 - 32 Stan G, King S W and Cook R F 2012 Nanoscale mapping of contact stiffness and damping by contact resonance atomic force microscopy *Nanotechnology* **23** 215703
 - 33 Kopycinska-Muller M, Yeap K -B, Mahajan S, Kohler B, Kuzeyeva N, Muller T, Zschech E and Wolter K -J 2013 Mechanical characterization of nanoporous materials by use of atomic force acoustic microscopy methods *Nanotechnology* **24** 355703
 - 34 Stan G, Gates R S, Kavuri P, Torres J, Michalak D, Ege C, Bielefeld J and King S W 2014 Mechanical property changes in porous low- k dielectric thin films during processing *Appl. Phys. Lett.* **105** 152906
 - 35 Stan G and Gates R S 2014 Intermittent contact resonance atomic force microscopy *Nanotechnology* **25** 245702
 - 36 Shekhawat G S and Dravid V P 2005 Nanoscale imaging of buried structures via scanning near-field ultrasound holography *Science* **310** 8992
 - 37 Tetard L, Passian A and Thundat T 2010 New modes for subsurface atomic force microscopy through nanomechanical coupling *Nat. Nanotech.* **5** 105
 - 38 Ebeling D, Eslami B and Solares S D 2013 Visualizing the subsurface of soft matter: simultaneous topographical imaging, depth modulation, and compositional mapping with triple frequency atomic force microscopy *ACS Nano* **7** 1038796
 - 39 Kimura K, Kobayashi K, Matsushige K and Yamada H 2013 Imaging of Au nanoparticles deeply buried in polymer matrix by various atomic force microscopy techniques *Ultramicroscopy* **133** 419
 - 40 Gaboriaud F and Dufrene Y F 2007 Atomic force microscopy of microbial cells: Application to nanomechanical properties, surface forces and molecular recognition forces *Colloids and Surfaces B: Biointerfaces* **54** 1019
 - 41 Spitzner E C, Riesch C and Magerle R 2011 Subsurface imaging of soft polymeric materials with nanoscale resolution *ACS Nano* **5** 315-320
 - 42 Roduit C, Sekatski S, Dietler G, Catsicas S, Lafont F and Kasas S 2009 Stiffness tomography by atomic force microscopy *Biophysical Journal* **97** 674677
 - 43 Stan G, Solares S D, Pittenger B, Erina N and Su C 2014 Nanoscale mechanics by tomographic contact resonance atomic force microscopy *Nanoscale* **6** 962-9
 - 44 Chawla J S, Singh K J, Michalak D J, Schenker R, Jezewski C, Krist B, Gstrein F, Indukuri T K and Yoo H J 2014 Patterning challenges in the fabrication of 12 nm half-pitch dual damascene copper ultra low- k interconnects *Proc. SPIE* **9054** 905404-8
 - 45 Bailey S, Mays E, Michalak D J, Chebiam R, King S and Sooryakumar R 2013 Mechanical properties of high porosity low- k dielectric nano-films determined by Brillouin light scattering *J. Phys. D: Appl. Phys.* **46** 045308-7
 - 46 Dubois G and Volksen W 2012 Low- k materials: Recent advances *Advanced Interconnects for ULSI Technology*, edited by Baklanov M R, Ho P S and Zschech E (Wiley Online Library, 2012), pp. 133
 - 47 Lomonosov A M, Ayouch A, Ruello P, Vaudel G, Baklanov M R, Verdonck P, Zhao L and Gusev V E 2012 Nanoscale noncontact subsurface investigations of mechanical and optical properties of nanoporous low- k material thin film. *ACS Nano* **6** 1410-5
 - 48 Stan G and Adams G G 2016 Adhesive contact between a rigid spherical indenter and an elastic multi-layer coated substrate *Int. J. Solids Structures* **87** 110
 - 49 Sergici A O, Adams G G and Muftu S 2006 Adhesion in the contact of a spherical indenter with a layered elastic half-space *J. Mech. Phys. Solids* **54** 1843-61
 - 50 Maugis D 1992 Adhesion of spheres: the JKR-DMT transition using a Dugdale model *J. Colloid Interface Sci.* **150** 243-69
 - 51 Johnson K L, Kendall K and Roberts A D 1971 Surface energy and the contact of elastic solids *Proc. R. Soc. London A* **324** 301-13
 - 52 Wahl K J, Asif S A S, Greenwood J A and Johnson K L 2006 Oscillating adhesive contacts between micron-scale tips and compliant polymers *J. Colloid Interface Sci.* **296** 178-88
 - 53 Constantinescu A, Korsunsky A M, Pison O and Oueslati A 2013 Symbolic and numerical solution of the axisymmetric indentation problem for a multilayered elastic coating *Int. J. Solids Struct.* **50** 2798-807
 - 54 Jakes J E, Frihart C R, Beecher J F and Moon R J 2008 Experimental method to account for structural compliance in nanoindentation measurements *J. Mater. Res.* **23** 1113-27
 - 55 Matsuda Y, Ryu I, King S W, Bielefeld J and Dauskardt R H 2013 Toughening thin-film structures with ceramic-like amorphous silicon carbide films *Small* **10** 253-257
 - 56 Yonekura K, Sakamori S, Goto K, Matsuura M, Fujiwara N and Yoneda M 2004 Investigation of ash damage to ultralow- k inorganic materials *J. Vac. Sci. Technol. B* **22** 548-53
 - 57 Cheng Y L, Huang J F, Chang Y M and Leu J 2013 Impact of plasma treatment on structure and electrical properties of porous low dielectric constant SiCOH material *Thin Solid Films* **544** 537-40
 - 58 Iacopi F, Stucchi M, Richard O and Maex K 2004 Electrical equivalent sidewall damage in patterned low- k dielectrics *Electrochem. Solid-State Lett.* **7** G79-82

Nanoscale tomographic reconstruction of the subsurface mechanical properties of low- k high-aspect ratio patterns

Gheorghe Stan,^{1,2} Ebony Mays,³ Hui Jae Yoo,⁴ and Sean W. King³

¹*Material Measurement Laboratory, National Institute of Standards and Technology, Gaithersburg, MD 20899, USA*

²*School of Engineering and Applied Science, George Washington University, Washington, DC 20052, USA*

³*Logic Technology Development, Intel Corporation, Hillsboro, OR 97124, USA*

⁴*Components Research, Intel Corporation, Hillsboro, OR 97124, USA*

Supplementary data

A. Tip shape characterization

The radius of the tip was determined by deconvoluting an average tapping mode AFM trace obtained from a post-measurement image (refer to Fig. S1) over the area where the measurements were performed. In this simulation a spherical tip was brought into contact with the profile of the fins; both tip and fins were considered rigid. The fins were modeled as rectangular shapes centered at the maximum heights that were observed in the actual average AFM trace. The widths of both thin and wide fins and the tip radius were considered variables in this fit procedure. For the optimal fit, a few intermediate positions are shown in Fig. S2 as the tip was scanned from left to right over the fins. In this case, a coefficient of determination of 97.0 % was calculated for the regions in between the fins. The main exercise here was to determine the tip radius from the regions in between the fins because, unlike on top of the fins, the tip imprints its apex curvature into the measured AFM trace around the edges of the fins. Along with the tip radius, the widths of the fins were determined as being 21 nm (narrow fins) and 90 nm (wide fins), respectively. No roundness for the corners of the fins was found necessary to be considered. Indeed, when corners of a few nanometers were assumed for the fins, the simulated AFM traces deviated significantly from the measured AFM trace, with large distortions in between the fins and in terms of the observed fin widths.

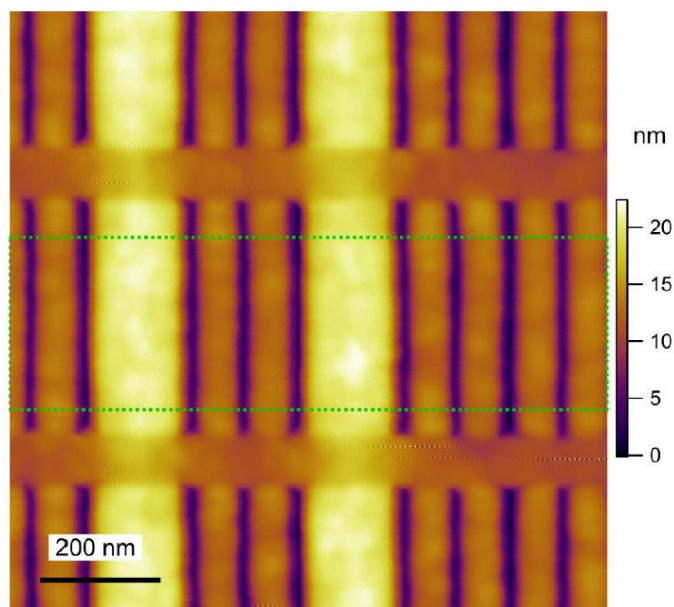


Figure S1: AFM topography of ILD fins after the measurements. The highlighted area was used to calculate the average AFM profile over these ILD fins.

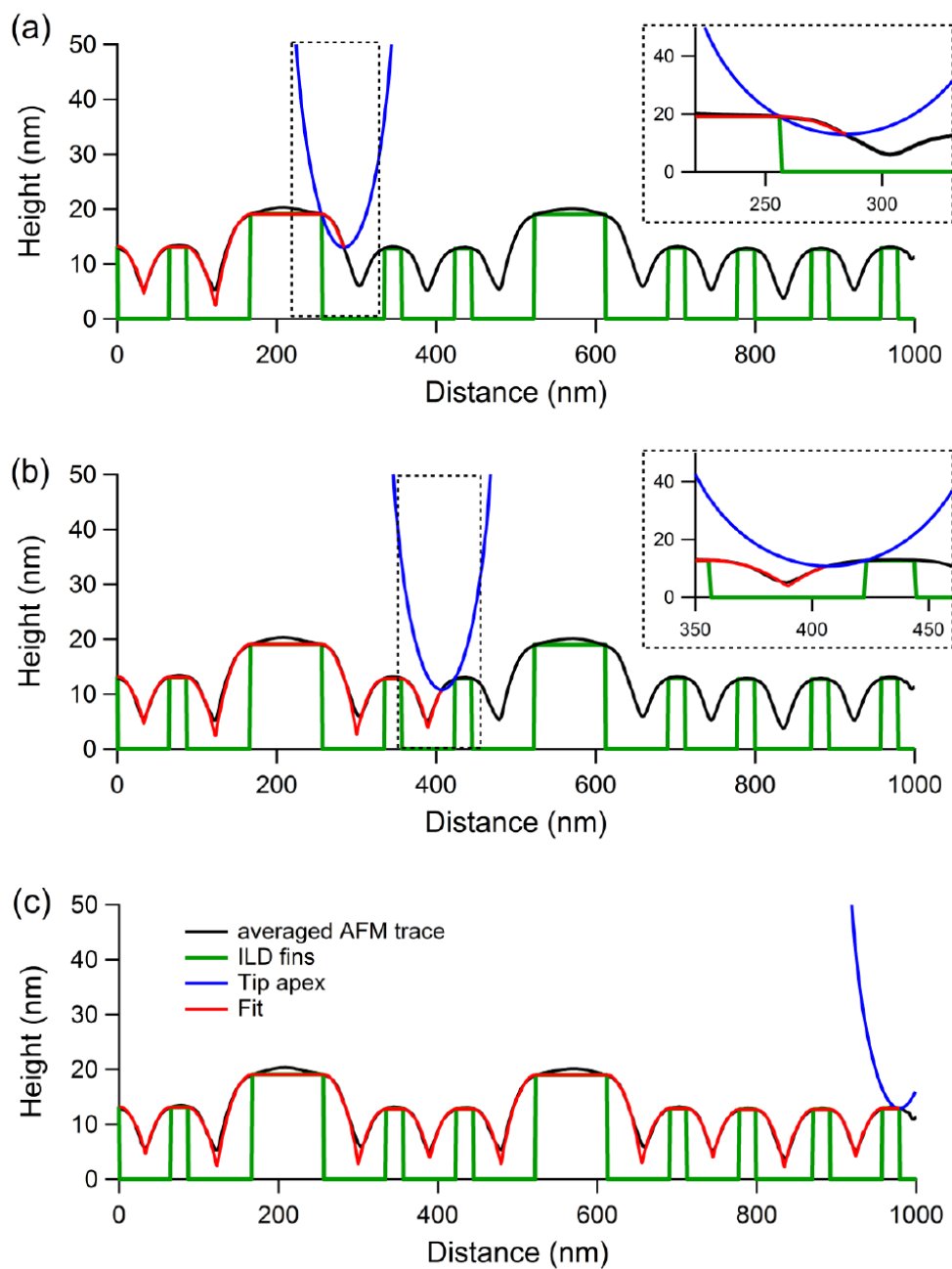


Figure S2: Tip radius calculation from the deconvolution of the AFM profile determined by averaging the scan traces within the highlighted area shown in Fig. S1. As the tip was scanned over the fins from left to right, intermediate positions are shown in (a), (b), and (c), respectively. The apex of the tip appears parabolic due to the different scales used on the x and y axes. A more detailed, proportional scaling is shown in the insets of (a) and (b).

B. Fits of contact stiffness versus force curves for different elastic modulus profiles

In Fig. S3 are shown a few fits of the contact stiffness versus force measurements at different locations over the wide fin, far away from its edges. Two possible cases were considered here, one with inhomogeneous fins made of a stiffer top cap and more compliant inner parts (variable elastic modulus) and one with homogeneous fins (constant elastic modulus). As explained in the main text, three variables were used to define a given configuration of an elastically inhomogeneous fin, E_B for the elastic modulus of the inner part, E_s for the elastic modulus of the top part, and z_c for the thickness of the top part, respectively, and only one variable, E , for the elastically homogeneous fins. As can be seen in Fig. S3, the fit with three parameters gave the correct observed force dependence of the contact stiffness whereas no good match could be obtained when the fins were assumed homogeneous. It is worth pointing out here that such fits are possible when the contact stiffness is measured over a range of forces to observe the stiffness response from zero to the maximum applied force. However, in CR-AFM measurements performed at a single applied force, the interpretation would indicate the elastic modulus for which the calculated contact stiffness will match the measurement at that particular force but, as can be seen in Fig. S3, this might be off for any other applied force.

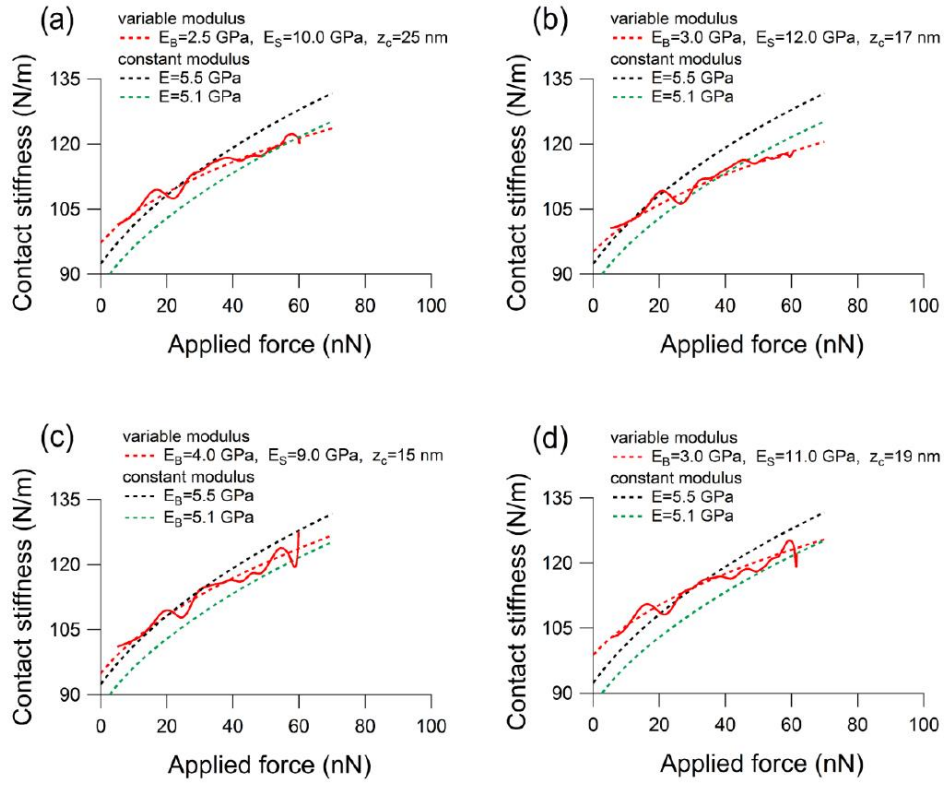


Figure S3: Examples of contact stiffness versus force fits over a wide fin in two considered cases: the fin is considered either inhomogeneous (variable elastic modulus by red dashed curves) or homogeneous (constant elastic modulus by black and green dashed curves) material. The coefficient of determination for the shown fits with variable modulus (red dashed curves) was (a) 96.8 %, (b) 96.0 %, (c) 94.1 %, and (d) 92.3 %, respectively.

C. Maximum stress under indenter in the JKR model

For the purpose of demonstration only we used here the JKR model to calculate the maximum compressive stress under the AFM tip during our ICR-AFM measurements on top of the wide low- k dielectric fins. This is because, with the parameters found by the semi-analytical procedure described in the text, we found that the JKR model provides close values for the maximum compressive stress compared to the ones calculated numerically. And, unlike the numerical procedure, the JKR model offers closed-form analytical expressions for the quantities of interest. Thus, in the JKR model, the stress distribution under a spherical rigid indenter of radius R pressed by a load P against a flat surface of a half-space of Young's modulus E and Poisson's ratio ν is given by

$$\sigma(r) = \frac{2E^*}{\pi R} \sqrt{a^2 - r^2} - \sqrt{\frac{2E^* a \Delta\gamma}{\pi(a^2 - r^2)}}, \quad (\text{S1})$$

where $E^* = E/(1-\nu^2)$, a is the contact radius, r is the radial distance from the center of the indenter, and $\Delta\gamma$ the adhesion energy. Upon the integration over the contact area, the load is found as

$$P = \frac{4E^* a^3}{3R} - 2\sqrt{2\pi E^* a^3 \Delta\gamma}, \quad (\text{S2})$$

with the minimum load identify as the pull-off force

$$P_c = -\frac{3}{2}\pi R \Delta\gamma \quad (\text{S3})$$

occurring at the minimum contact radius

$$a_c = \sqrt[3]{\frac{9\pi R^2 \Delta\gamma}{8E^*}}. \quad (\text{S4})$$

The maximum compressive stress happens at the center of the indenter at $r = 0$:

$$\sigma(0) = \frac{2E^* a}{\pi R} - \sqrt{\frac{2E^* \Delta\gamma}{\pi a}}. \quad (\text{S5})$$

By using (S5) and (S2), the load dependence of $\sigma(0)$ was plotted in Figure S4 for the case of interest with $R = 67$ nm, $E = 8$ GPa, $\nu = 0.25$ and $|P_c| = 20$ nN. As it can be seen from Figure S4, the maximum compressive stress $\sigma(0)$ is about 0.6 GPa at an applied load of 60 nN (maximum applied load during measurements), which was rationalized to be below the yield stress of these

materials. While we didn't directly measure the yield stress of the materials used in this work, we can indirectly estimate it somewhere close to 1.0 GPa. The estimate is based on the yield stress measurements of SiCH/SiOCH bilayers,⁵⁵ with the SiOCH layers having similar structure and properties (porosity 25 % and elastic modulus 8.0 GPa) to our materials. In these measurements it was found that the top SiCH layers can accommodate yield stresses as high as 1.0 GPa depending on their porosity. Based on the observation that plasticity was always initiated in the SiCH layer we can conclude that the yield stresses of the SiOCH layers are even higher than those of the SiCH layers.

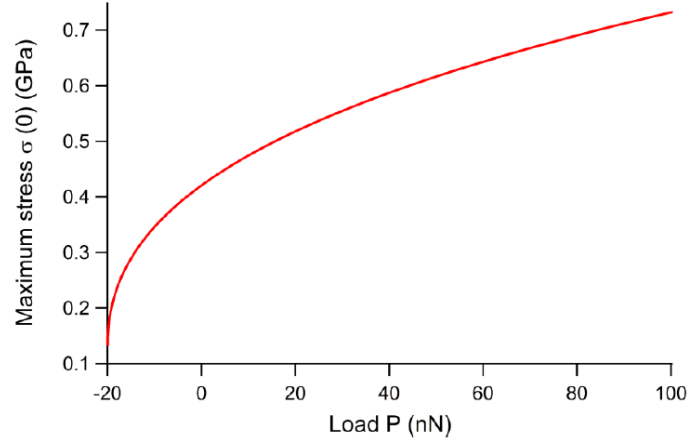


Figure S4: Load dependence of the maximum compressive stress under the indenter in the JKR model as applied to the case of ICR-AFM measurements performed on top of the wide fins (refer to the main text for the values of the parameters used in experiments).